Journal of Power Sources 194 (2009) 541–549

Contents lists available at ScienceDirect

Journal of Power Sources

journal homepage: www.elsevier.com/locate/jpowsour

Identify capacity fading mechanism in a commercial $LiFePO_4$ cell

Matthieu Dubarry, Bor Yann Liaw*

Hawaii Natural Energy Institute, SOEST, University of Hawaii at Manoa, 1680 East-West Road, POST 109, Honolulu, HI 96822, USA

ARTICLE INFO

Article history:
Received 17 April 2009
Received in revised form 18 May 2009
Accepted 20 May 2009
Available online 27 May 2009

Keywords:
$LiFePO_4$
Cycle life evaluation
Capacity fade
Peak power capability
Incremental capacity analysis
Li inventory loss

ABSTRACT

The capacity fading of an 18650 $LiFePO_4$-based lithium ion cell was studied using the dynamic stress test (DST) schedule in a cycle life evaluation. Intermittent reference performance tests were conducted to quantify capacity loss and peak power capability degradation with cycle number to the end-of-life. An incremental capacity analysis was applied to identify various contributions to capacity loss, whereas the open circuit voltage measurements were utilized to trace the correct state of charge as the cell degrades in order to accurately correlate the capacity degradation with SOC. Our non-invasive, *in situ* analyses are in general consistent with current understanding of the degradation mechanism in this chemistry derived from post-mortem analysis. Loss of lithium inventory is the main cause of capacity degradation, in addition to the loss of active materials. The degree of under-discharge and under-charge is quite minimal under the test protocol.

1. Introduction

$LiFePO_4$ (LFP)-based cell chemistry has been extensively studied and developed in the past few years because of its promise as a safe and cost-effective cathode material for the next generation of Li ion battery applications. Indeed it presents high rate capability, high specific capacity (170 mAh g^{-1} [1]), good safety attribute, attractive cost competitiveness, and low toxicity [1–7]. To date, there are quite a few manufacturers producing $LiFePO_4$-based rechargeable lithium ion cells for portable electronics, power tools and electric and hybrid vehicle applications. But, to our knowledge, few reported the degradation mechanisms [8] in these commercial cells in open literature, although many of the commercial electrode materials have been investigated in the laboratories [5–7,9].

Characterizing capacity degradation in a commercial battery relies on life testing using a defined procedure and protocol such as those proposed by the U.S. Advanced Battery Consortium (USABC) electric vehicle battery test procedures manual [10] and subsequent modifications for hybrids and plug-in hybrids. Although these standardized procedures can quantify capacity fade in controlled environments, the results were not useful to provide sufficient knowledge of the degradation mechanism in commercial cells in practical applications. Some traces of degradation can be revealed by post-mortem analyses [5,6]; however, the results are less informative to offer any temporal correlation of the degree of fading with underlying mechanism.

This temporal correlation of capacity fade and degradation mechanism is a key to safe and reliable battery operation, since the battery management system needs to be able to detect anomalies and possible failure as early as possible. It is therefore important to develop *in situ* methods to monitor the cell behavior accurately without having to put the power source system to maintenance check. Such non-invasive methods also need to be sufficiently efficient for the on-board control electronics with minimal computation. We recently developed [11–14] a useful approach that employs incremental capacity analysis (ICA) [12,15–17] and close-to-equilibrium OCV (*cte*-OCV) [12–14] measurements to trace the SOC changes of a battery in order to analyze capacity fade detected in the cycle life tests and to decipher its origin. Using this approach, we were able to quantify capacity degradation in the cells through the analysis of voltage–current response.

This paper is to present such an analysis of a commercial $LiFePO_4$ cell solely relying on these *in situ*, non-invasive methods and based on the data acquired from the standard test procedures. It is important to note that the scope of this paper is not to clarify or validate any intercalation theory or degradation mechanism, as a number of outstanding studies [18–21] have already been reported in the literature. Our goal is to illustrate that the non-invasive methods described below, combined with the reported key evidence of possible degradation mechanisms in the literature, can provide a powerful diagnosis tool for commercial cells.

2. Experimental

A group of 1.45 Ah $LiFePO_4$-based 18650 cells was provided by a commercial vendor for evaluation using a Solartron 1470 test

* Corresponding author. Tel.: +1 808 956 2339; fax: +1 808 956 2336.
E-mail address: bliaw@hawaii.edu (B.Y. Liaw).

0378-7753/$ – see front matter © 2009 Elsevier B.V. All rights reserved.
doi:10.1016/j.jpowsour.2009.05.036

station. One of the cells was subjected to the USABC EV battery core tests followed by a cycle life test using the dynamic stress test (DST) schedule in the cycle aging. After every 50 DST cycles, the cell was characterized by the reference performance test (RPT) to determine changes in the rated capacity (C_n to denote the capacity measured at the C/n rate) and peak power capability (PPC).

The DST schedule and the RPT test protocols (which comprise constant current, constant power, variable power, and peak power discharges) have been described in details in our previous work [13]. The results presented in this work were extracted from the cell cycled between 3.65 and 2 V and charged with a regimen consisted of a constant current at C/2 and a constant voltage trickle charge cut-off at C/20. Although it was an evaluation of a single test cell, the results were representative for the specific chemistry tested. To verify hypotheses deduced from the incremental capacity analysis of this test cell, we also conducted additional experiments using another cell of the same batch to provide more data and evidence for validation.

3. Results

3.1. Capacity retention upon cycling: DST versus constant current regimes

Prior to the cycling test four conditioning cycles at C/3 were performed on the cell and the rated capacity C_3 was measured to be 1.218, 1.204, 1.199 and 1.195 Ah, respectively; thus, a mean $C_3 = 1.204 \pm 0.010$ Ah was measured, 18% less than the nominal $C_2 = 1.45$ Ah specified by the manufacturer. This has been verified to be the same for all the cells provided to us. Such a discrepancy led us to redefine the rated capacity of the cell based on $C_3 = 1.20$ Ah as the initial state of the battery as received for subsequent testing and evaluation. The cell exhibits a specific capacity of 33 Ah kg^{-1} based on the total weight of the cell.

Fig. 1 presents the evolution of the capacity retention upon DST cycling (◯) along with C_5, C_3, C_2 and C_1, determined by RPTs. By contrast, the discharge regime under the DST schedule, which should be close to a 5-h rate, delivered only about 82% of C_5. The lower capacity in C_{DST} than C_5 is likely due to a much earlier cut-off in the DST regimen, because the schedule comprises a high discharge pulse of about 1.5 C that often triggered an early termination at the same end-of-discharge voltage (EODV).

The USABC procedures define the end-of-life of a battery when it cannot deliver more than 80% of its rated capacity under a specific test protocol. Since we adopted $C_3 = 1.20$ Ah as the initial nominal rated capacity, the cell thus reached end-of-life (80% of $C_3 = 1.20$ Ah) after 450 cycles. Up to the 400th cycle the capacity fading was similar for all the rates tested (about 17% from their respective initial capacity). After 400 cycles, the fading for all rates increased and some disparity in the rate of fading began to appear. The capacity fading accelerated more at higher rates (i.e., C/1 and DST), leading to about 45% loss for the lower rates and more than 60% loss for the higher ones after 600 cycles.

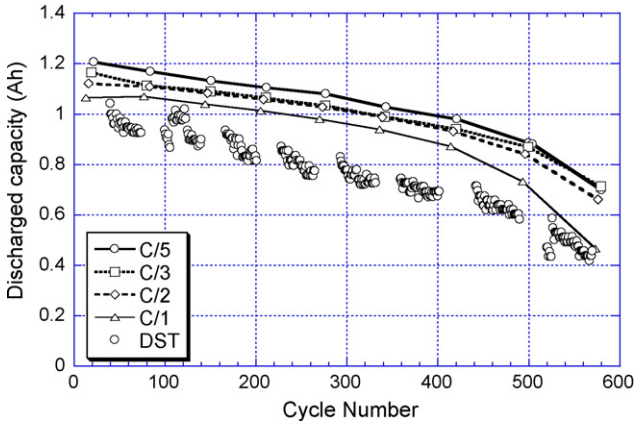

Fig. 1. Capacity determined in the DST cycling and in the C/5, C/3, C/2 and C constant current tests in reference performance tests.

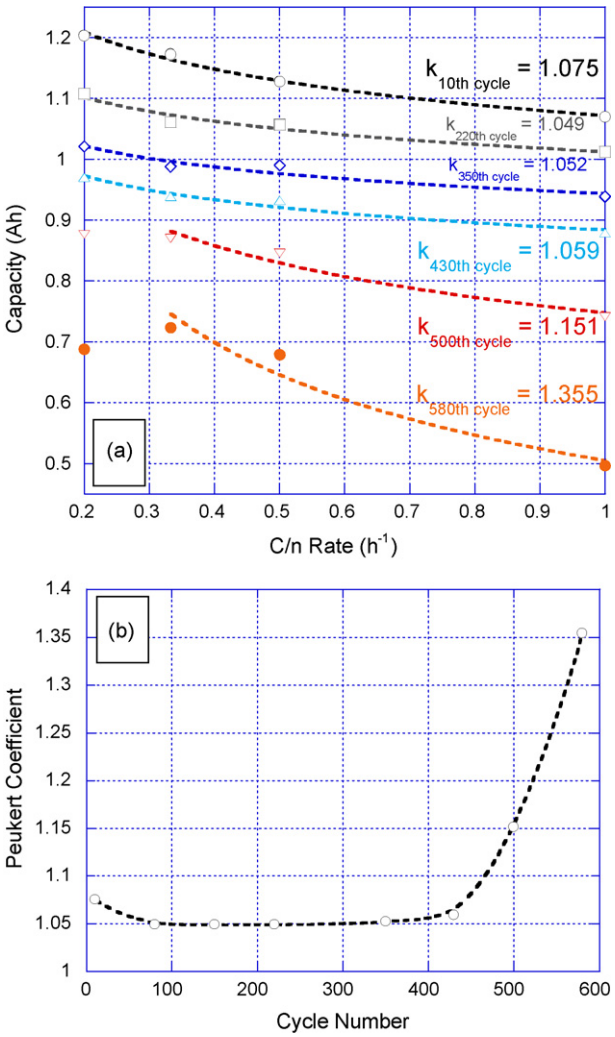

Fig. 2. Evolution of (a) the Peukert curve and (b) the Peukert coefficient in the DST cycle aging.

Fig. 2(a) shows the Peukert curves at various stages of life (in cycle number), and Fig. 2(b) the Peukert coefficient variations with cycle number, which depicts the capacity retention pattern. The Peukert coefficients were derived from the Peukert curves in Fig. 2(a), as depicted by the Peukert's law, $C = I^n t$; where n is the Peukert coefficient and t the nominal discharge time (in hours) for a specific C-rate (in Amperes). The reliability factors of the fits for all the curves are superior to 97% to the 430th cycle. The reliability factors decrease to 90% and 80%, respectively, at the 500th and 580th cycle because C_5 is unexpectedly low (as explained later in Section 4.3.3). In light of possible artifact, the curves have been fit without C_5 and the reliability factors increased to values superior to 97%, comparable to those of earlier cycles for comparison as follows.

The profile in Fig. 2(b) indicates that the Peukert coefficient declines gradually from the 1st to the 80th cycle and remains relatively constant throughout the remaining 320 cycles. After 400 cycles, the Peukert coefficient begins to increase at a noticeable pace.

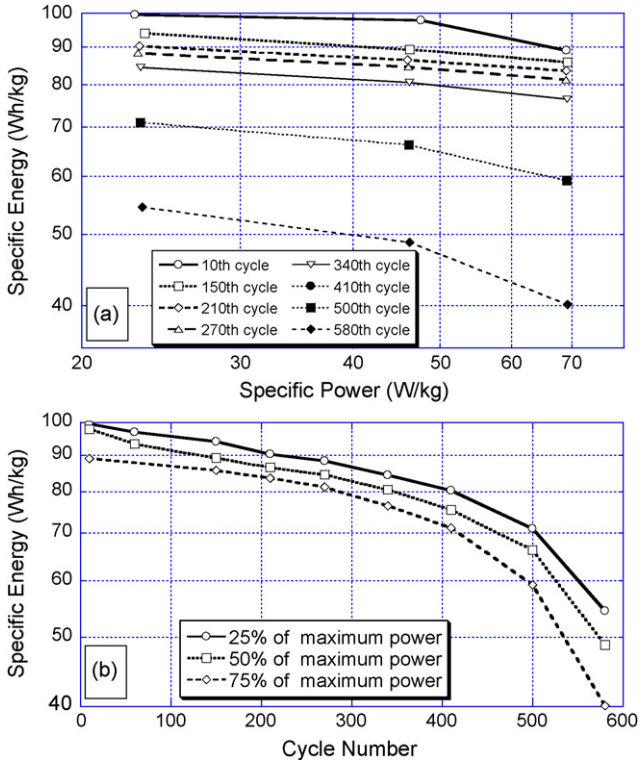

Fig. 3. Evolution of (a) the Ragone plot and (b) the specific energy in the DST cycle aging.

3.2. Power capability retention: Ragone plot and peak power test

The power capability of the cell is presented by two representations (from two different test protocols). One is the Ragone plot that reveals the trade-off of specific energy (Wh kg^{-1}) versus specific power (W kg^{-1}). The data used in the construction of the Ragone plot is based on the energy attainable from the cell measured at various constant power discharge regimes, typically at 25%, 50%, and 75% of the USABC power goal in W kg^{-1}. The resulting Ragone curves obtained from the sequential RPT studies are shown in Fig. 3(a). The highest specific power tested was 70 W kg^{-1}. The curves follow a downward trend, displaying the specific energy degradation through the cycle aging as shown in Fig. 3(b). Through the first 400 cycles a specific energy better than 70 Wh kg^{-1} was attainable even if the specific power went up to 70 W kg^{-1}. Beyond 400 cycles, the cell began to show noticeable specific energy degradation. Although the specific energy at 23 W kg^{-1} was still acceptable (i.e., >70 Wh kg^{-1}), the cell could not deliver more than 60 Wh kg^{-1} if the power demand was increased to >70 W kg^{-1} after 500 cycles. After 580 cycles, the cell could not deliver more than 55 Wh kg^{-1} even at 23 W kg^{-1}.

The second representation of the power capability is depicted by the peak power capability (PPC) profile of the cell, as described by the ability of the battery to produce 30 s of peak power (roughly at 3.9 C) without lowering the voltage to below 2/3 of the OCV at the specific SOC [10]. The evolution of PPC as a function of DOD upon cycling is shown in Fig. 4(a). The PPC was decreasing slowly in the first 400 cycles. The degradation became severe after that. After 500 cycles only less than 50% of the initial rated capacity is attainable.

The polarization resistance was estimated from the $\Delta V/\Delta I$ that was measured between the base and the peak power steps. This resistance and the PPC at 0% DOD (when the battery was fully charged according to the manufacturer's specifications, which is not necessarily representing 100% SOC) are plotted as a function of

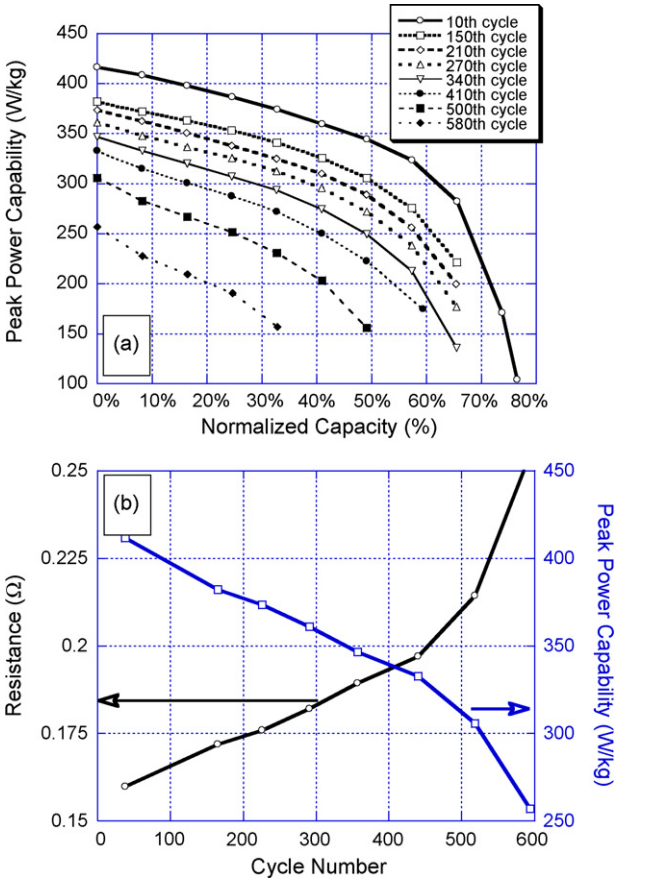

Fig. 4. Evolution of (a) the peak power capability and (b) the PPC at fully charged state and of the internal resistance in the DST cycle aging.

cycle number in Fig. 4(b). The resistance was doubled in the first 400 cycles. After 400 cycles, the resistance increases at a higher pace, double in less than 150 cycles. We unfortunately do not have the actual electrode area to derive the area specific impedance values in this report.

3.3. Close-to-equilibrium OCV measurements

The close-to-equilibrium OCV (*cte*-OCV) measurements can provide accurate estimates of the SOC of the cell to allow us trace the SOC profile and its progression with aging. Tracing SOC accurately is a vital requirement for safe and reliable battery management and operation and will allow us to correctly correlate the degradation phenomena with the operating conditions. As a baseline comparative sample, a second cell of similar capacity and polarization characteristics has been cycled at C/25, as shown in Fig. 5. Testing at C/25 is the best compromise between time and accuracy. The result allows us to yield a practical capacity close to the maximum attainable, thus we can use such a capacity to derive the SOC versus Ah relationship with minimal polarization effects. We used this approach to define a '*pseudo*-OCV' versus SOC curve. The *pseudo*-OCV is the mean of the voltages on C/25 charge and discharge curves. Although this approach is an approximation to the correspondence of the staging phase transformations in the anode, it is accurate enough in the high and low SOC regions where we need to trace the *cte*-OCV for SOC estimate.

Fig. 6(a) presents the variations of the *cte*-OCV at the end of relaxation at the end-of-discharge (EOD) and end-of-charge (EOC) as a function of cycle number for the constant current (at various

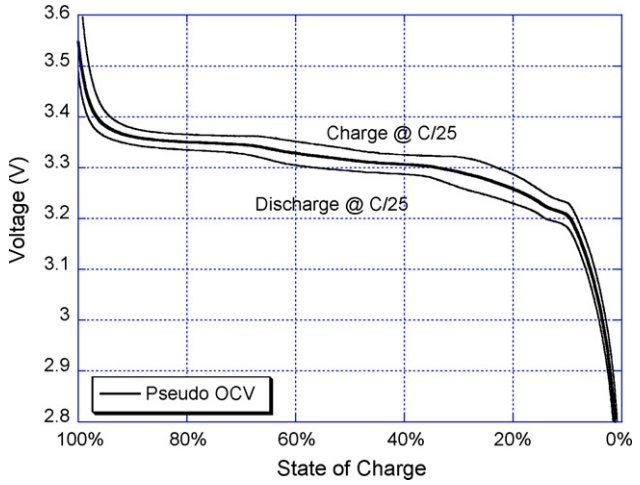

Fig. 5. C/25 charge and discharge curve of a cell different from the test cell and the '*pseudo*-OCV' versus SOC curve.

rates) and DST cycles. It is interesting to note that the *cte*-OCV at the end-of-discharge in the constant current cycles all decreased in the first 80 cycles. After 80 cycles, the *cte*-OCV at the end-of-discharge stabilized and gradually began to increase with cycle, especially after 400 cycles and for higher rates. In contrast, the *cte*-OCV at the end-of-discharge (EOD) for the DST cycle aging (o) remained nearly constant, or slightly increased with cycle, suggesting a very minute under-discharge. A close look of these *cte*-OCVs

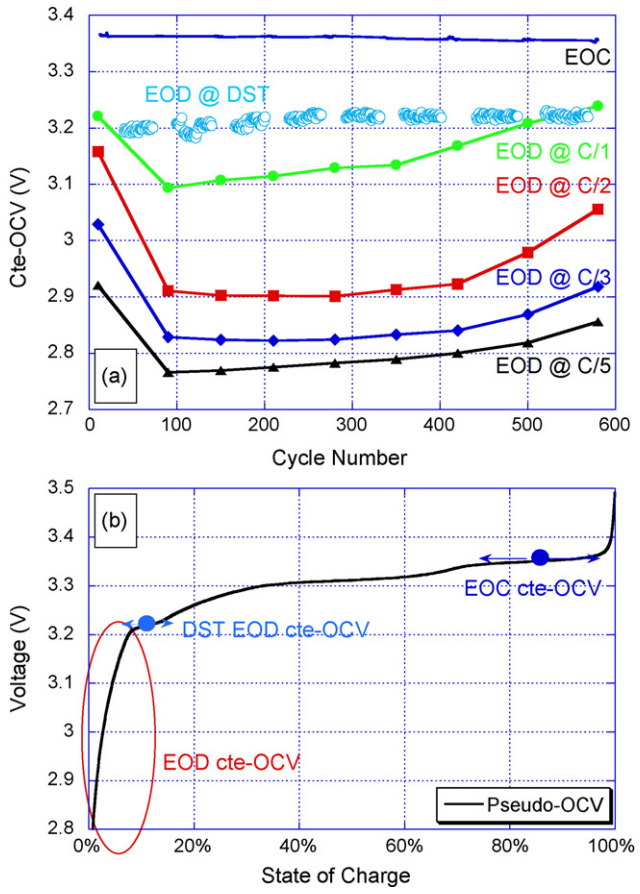

Fig. 6. (a) Variation of the relaxed cell voltage during cycling and at different rates determined in the reference performance tests, and (b) projection of the relaxed cell voltage ranges on the *pseudo*-OCV versus SOC curve.

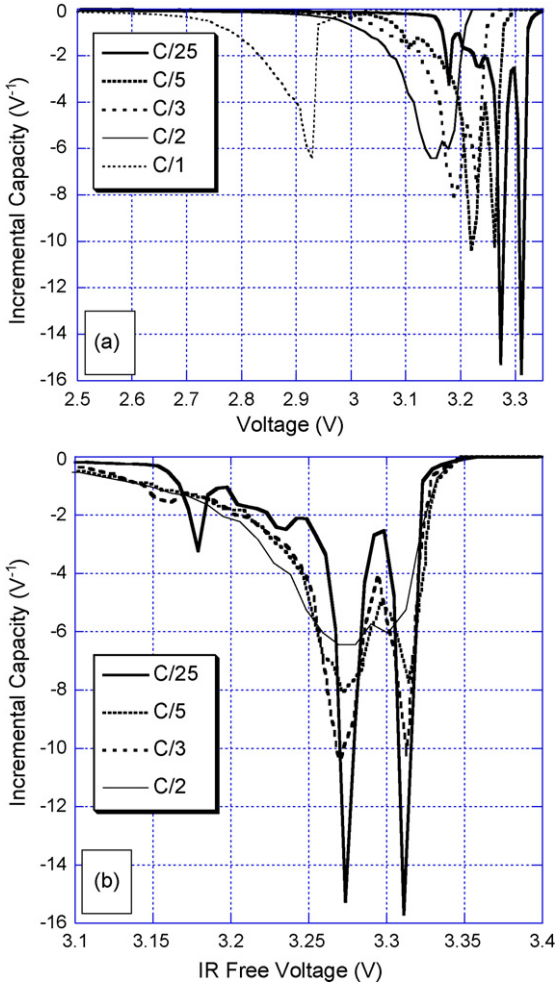

Fig. 7. Incremental capacity peaks calculated from the discharge curves of various rates and (b) the same peaks with a polarization correction.

on the *pseudo*-OCV versus SOC curve indicates that they are located on a voltage plateau; therefore, the *cte*-OCV could not help us decipher if it is feasible or accurate for SOC tracing (Fig. 6(b)). Since the plateau length would not span over 5% of SOC, it gives a good faith estimate of the maximum variation in the end-of-discharge SOC, which should be <5%. In the charge regime the same situation occurs as the *cte*-OCV at the end-of-charge (EOC) is also on a long voltage plateau. This is disappointing to us in the attempt to estimate the end-of-charge SOC using the *cte*-OCV and preventing us to estimate the under-charge quantitatively.

3.4. Incremental capacity variations

The incremental capacity (IC) depicts a capacity change associated with a voltage step ($\Delta Q/\Delta V$). Each peak in the incremental capacity curve has a unique shape, intensity, and position, and it exhibits an electrochemical process taking place in the cell. Fig. 7 shows the incremental capacity peaks derived from the discharge curves at various rates, and (a) is with and (b) without the polarization. The C/25 discharge curve was measured from another cell and the corresponding incremental capacity curve is included as a reference. The five peaks observed in the incremental capacity curves correspond to the staging in the graphite negative electrode, convoluted with a single and very broad plateau of the $FePO_4$ (FP)–$LiFePO_4$ (LFP) phase transformation on the positive electrode [5,6,11,21]. The solid solution region of the terminal phases in $FePO_4$

and $LiFePO_4$ were not observed as it is known that large-grain positive electrode only exhibits a very limited stoichiometry in the solid solution regions [18,19,22]. We have tested a few $LiFePO_4$ commercial cells from different vendors, and more detailed discussion of the grain size effects and solid solution aspects will be reported elsewhere [11].

To develop a better understanding of the incremental capacity behavior with this chemistry, we first have to eliminate the polarization effects. The potential shift of an incremental capacity peak with various rates (in Fig. 7(a)) gives an estimate of the polarization resistance of the cell. In order to estimate the polarization resistance, we use the data in the linear region of the Tafel equation; thus, only rates less than C/1 were used in the calculation, which gives a reliability factor of 99.2%. Such a resistance was estimated to be 0.19 Ω, which is in good agreement with that calculated from the peak power capability experiments (0.16 Ω) at the initial state. Knowing the resistance, we can eliminate the polarization effect in order to provide the ease of comparison among the incremental capacity peaks derived from various rates (Fig. 7(b)). We should note that the charge branch of the C/25 incremental capacity curve is different from the rest using the (CC-CV) algorithm recommended by the manufacturer. Therefore, the intensity of the first incremental capacity peak (at 3.31 V) at C/25 cannot be used for comparison with the others at different rates in the discharge branch.

Although the polarization effects were eliminated from the peak position, Fig. 7(b) shows that the incremental capacity peaks remain broadened with increasing rate; thus, additional kinetic effects are still in play, and their impacts are not the same on every incremental capacity peak. The first peak at 3.31 V is far less affected as evident by the sharp peak shape, at least for the "up-ramping" slope of the peak, while its intensity decreases with increasing rate. The intensity decrease in other peaks cannot be explained solely by peak broadening, since the associated area under the peak is also shrinking. It is also interesting to note that the broadening does not induce any noticeable loss of capacity as the incremental capacity profile towards the end of the potential window both in discharge (2.5 V, in Fig. 7(a)) and charge (3.65 V, in Fig. 8(b)) is close to nil for all rates.

Fig. 8 depicts the incremental capacity curves associated with (a) discharge at C/5 and (b) charge at C/2 at the 10th, 160th, 300th, 430th, 500th and 580th cycles. In the discharge regime (Fig. 8(a)), the first incremental capacity peak at 3.27 V exhibits a more considerable intensity decrease than the other incremental capacity peaks, and the peak position slides with cycle until the peak becomes indiscernible after 430 cycles, indicating that the cell is progressively under-charged. The second (and the most prominent) incremental capacity peak is also sliding towards lower potentials, indicating a progressive increase of the polarization resistance. In the charge regime (Fig. 8(b)), there is also a peak position shift towards higher potentials, reflecting a corresponding polarization resistance increase similar to that in the discharge regime. From the incremental capacity curves presented in Fig. 8 we estimated the evolution of the resistance upon cycling in the discharge and charge regimes, as shown in Fig. 9. They are not symmetrical though, as the resistance in the charge regime is about twice of that of the discharge.

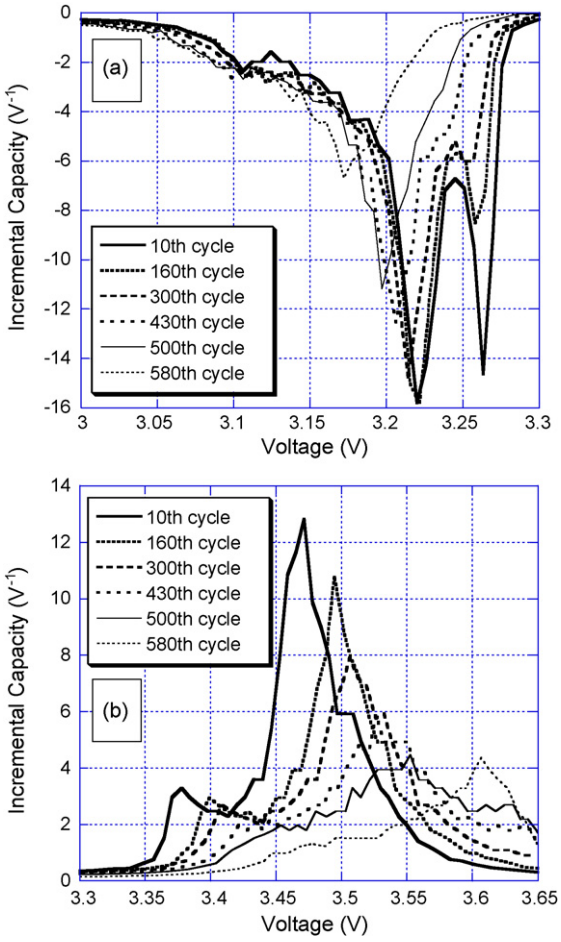

Fig. 8. Incremental capacity curves for (a) C/5 discharges and (b) C/2 charges as determined in the reference performance tests in the DST cycle aging.

4. Discussion

4.1. Capacity retention in cycle aging

The DST cycle aging revealed a complicated capacity retention behavior, which is rate-dependent, as shown in Fig. 2(a), and indicates that at various rates the cycle-dependent retention did not follow the same trend line. Fig. 2(b) further suggests that the overall retention behavior, as reflected by the Peukert's coefficient, is age-dependent. These observations suggest the following possibilities: (1) there might be more than one mechanism involved in the capacity retention in cycle aging, and their influence on the retention depends on the C-rate; or (2) it could be a single but complicated mechanism that makes the extent of retention rate- and age-dependent.

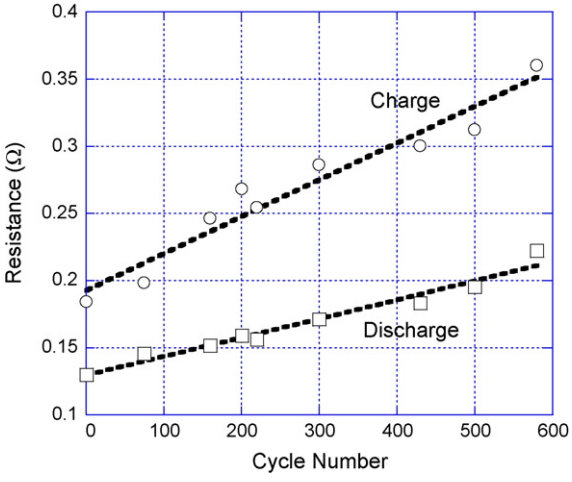

Fig. 9. Evolution of the polarization resistance in charge and discharge regimes as determined in the reference performance tests in the DST cycle aging.

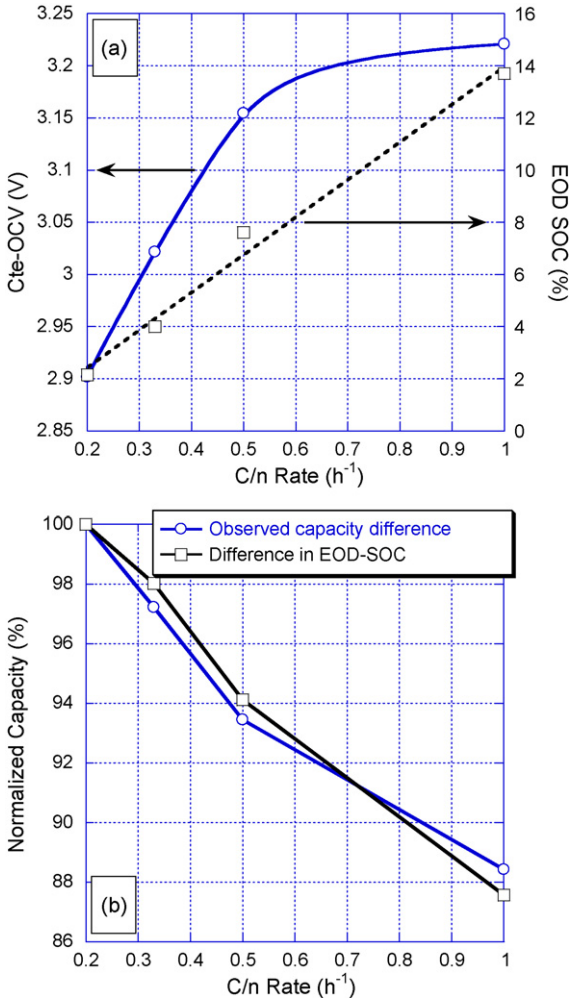

Fig. 10. (a) Difference in depth of discharge (DOD) as a function of the rate and (b) associated capacity difference compared to the difference in DOD.

4.2. Initial rate effect on capacity retention

Fig. 10(a) presents the variation of the end-of-discharge SOC (□) as estimated from the *cte*-OCV measurements. The relaxed cell voltage (○) was used to infer the SOC from the *pseudo*-OCV versus SOC curve (Fig. 5). It appears that the end-of-discharge SOC decreases with rate almost linearly. This linear rate-dependence in end-of-discharge SOC could account for more than 12% in capacity difference from C_1 to C_5. Fig. 10(b) shows the comparison between the end-of-discharge SOC and capacity variations with the rate, and, indeed, they agree well. Since for large-grain positive electrode the solid solution stoichiometry is very narrow in $FePO_4$ or $LiFePO_4$, the constant potential plateau at the positive electrode should extend to almost the entire composition range studied. The *cte*-OCV variations observed at different rates in Fig. 10(a) must be due to the potential variations at the negative electrode, as a result of different extent of reaction and residual amount of Li ions left in the electrode. The variations in the extent of reaction in the positive electrode, on the other hand, should not reflect in any potential variation in the cell voltage. This result is consistent with the general understanding that the rate limiting electrode is the negative one, since the $FePO_4$–$LiFePO_4$ phase transformation is facile [18–20] and replacement of the carbonaceous anodes by nano-$LiTiO_2$, for instance, can considerably enhance the maximum discharge rate [23].

4.3. Capacity retention at different stages of cell aging

To aid the discussion of capacity retention and fade, we would like to mention the four possible modes of capacity degradation, that include loss of active material (LAM), loss of Li inventory (LLI) due to parasitic side reactions, under-charge (UC), and under-discharge (UD). In principle, in the incremental capacity analysis, the loss of active material shall cause intensity of the incremental capacity peaks to decrease in proportion, while the loss of Li inventory in disproportion. The under-charge and under-discharge are likely the consequences of polarization increase, which result in the shifting of the incremental capacity peak position and subsequently driving a part of the electrochemical process (next to the potential window of interest) pre-maturely terminated. This portion of the reaction outside the potential window thus becomes inactive and the corresponding capacity becomes unavailable. This type of capacity loss is usually recoverable. The symptom observable in the incremental capacity analysis is evident by a gradual loss of the corresponding incremental capacity peak intensity without affecting the others. The loss can be recovered if the potential window were extended [12].

The principle discussed above can be used in the deciphering of the degradation mechanisms in the $LiFePO_4$ chemistry. To date, possible degradation mechanisms for the $LiFePO_4$ chemistry reported in the literature include: (1) Fe dissolution from the positive electrode in the presence of HF [24], which leads to Fe migration and deposition onto the negative electrode and destabilization of the SEI [9]; (2) loss of Li inventory, according to the post-mortem analyses of test cells [5,6], which was probably the result of the SEI destabilization [6,9] and resulted in an interfacial resistance increase at the negative electrode [5]; (3) loss of active material reported by Koltypin et al. [24] due to the formation of insulating LiF surface film on $LiFePO_4$ that leads to the isolation of some of the grains in the positive electrode. The LiF formation also increases positive electrode impedance.

Using the incremental capacity and *cte*-OCV analyses we were able to derive more information of the aging pattern associated with the DST cycling of this cell, as shown in Fig. 2. Among the three stages of capacity retention pattern observed, the second stage, where the Peukert coefficient is rather constant and the capacity retention is steady and linear, will be discussed first.

4.3.1. Stage two of capacity retention

Fig. 6(a) presents the evolution of the end-of-discharge relaxed cell voltage at various rates. The end-of-discharge SOC was then determined from the *pseudo*-OCV-SOC curve in Fig. 5. The amount of input charge was added to the end-of-discharge (EOD) SOC to estimate the end-of-charge (EOC) SOC as shown in Fig. 11. Although the end-of-charge SOC varies throughout the life of the cell; at any given cycle, the end-of-charge SOC is invariant to the discharge rate. This result corroborates our *cte*-OCV analysis and end-of-discharge SOC estimates, because the charge algorithm indeed recharged the cell to the same end-of-charge SOC. Therefore, we now have a complete set of consistent end-of-charge and end-of-discharge SOC for various rates over the entire cycle life for further analysis.

In this stage of capacity retention, the end-of-discharge SOC is almost invariant from 80 to 400 cycles for all rates. This observation immediately rules out the possibility of under-discharge for any capacity fade. On the other hand, the end-of-charge SOC declined in a steady manner for all rates at a rate of −0.04% SOC per cycle. This SOC tracing indicates that the capacity of the cell decreases through cycle aging, which agrees with the observation in Fig. 1. In Fig. 8(b), the incremental capacity results suggest that under-charge did not contribute to the decline of end-of-charge SOC in a significant manner, since the degree of under-charge is far less than the more severe intensity decline of the 3.27 V peak during

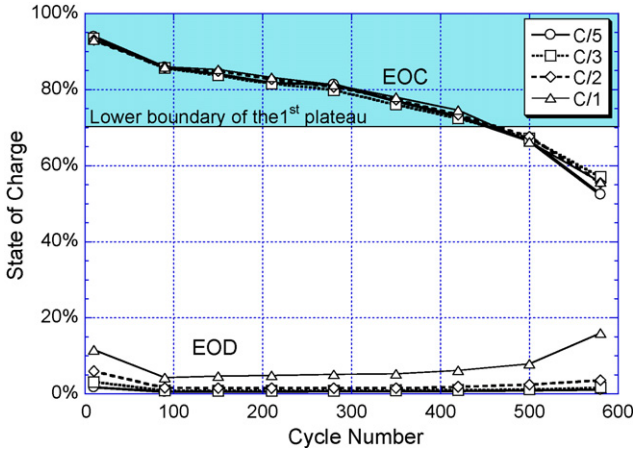

Fig. 11. Evolution of the end-of-charge and end-of-discharge SOC at various rates as determined in the reference performance tests in the DST cycle aging. Also shown is the SOC range of the first potential plateau derived from the corresponding *pseudo*-OCV versus SOC curve in Fig. 5.

discharge cycles. The observed end-of-charge SOC decline however can be explained by loss of Li inventory, a process that led to a less amount of Li returned to the negative electrode one cycle after another, while the end-of-discharge SOC remained the same. This explanation is consistent with the observed significant disproportional intensity decrease of the 3.27 V peak in contrast to that of the 3.22 V peak. The intensity decline of the 3.27 V peak from the 10th to the 160th cycle is quite profound, as shown in Fig. 8(a); while the change of the 3.22 V peak is essentially negligible during the same period. The evidence of loss of Li inventory is also supported by the proportional decrease in the peak height of both 3.37 and 3.47 V peaks in the charge branch concomitantly. The simultaneous peak position shifting for both peaks is indicative of the increasing SEI resistance as suggested by [9].

We should also note that through cycle aging, although the 3.27 V discharge peak position was gradually shifted (as a result of increasing polarization), its shape (at least the front descending slope of the peak) did not alter much until it began to disappear after 430 cycles. It indicates that the Li intercalation kinetics in the beginning of the discharge remained intact through aging. This is consistent with earlier studies reported in [5,6,9] that capacity degradation is most likely caused by interfacial problems, not bulk behavior.

We also observed that the broadening of the lower-potential (3.22 V and below) incremental capacity peaks in both discharge and charge regimes. This phenomenon may be related to the SEI destabilization and disorder of graphite surface over cycling [9] during discharge at low potentials. The SEI could be partly dissolved during charge. However, this process would not affect the discharge kinetics at high potentials too much. Such an SEI reformation has been suggested [9] for graphite anodes and also been observed for other positive electrode materials [25]. Such a postulation indeed might be the one that resulted in the loss of Li inventory. This side reaction might also lead to an accumulation of inorganic residual compounds of phosphates, carbonates, and LiF; thus increase the cell impedance as observed in Fig. 9.

Although loss of Li inventory is considered the major contribution to the capacity degradation, we still need to investigate if the loss of active material was an issue. In Fig. 8(a), the peak position and height of the 3.22 V discharge peak remain the same from cycle 10 to cycle 160 is an assertion that loss of active material did not play a role in the capacity degradation. After 300 cycles, this discharge peak began to shift its position and fade in height, while the corresponding charge peaks in Fig. 8(b) continue to exhibit the same pattern of peak shifting and proportional peak height reduction. These observations corroborate the belief that the loss of Li inventory remains active in capacity degradation and the primary source of capacity loss. The fact that the 3.27 V peak remains existing as a minor peak, while the 3.22 V peak height has decreased, indicating that the loss of active material indeed exists, but it is difficult to quantify at this stage.

4.3.2. *The first stage of capacity retention*

The first stage of capacity retention pattern was marked by the reduction of the Peukert's coefficient in the first 80 cycles, as shown in Fig. 2. This pattern of behavior is further characterized and exhibited in Fig. 11, in which decreasing trends in both end-of-charge SOC and end-of-discharge SOC for various rates were revealed.

The decline in the end-of-discharge SOC varies with rate in this stage, from 1.1% for C/5 to 5.5% for C/2. The charge algorithm was able to return the charge properly to the same end-of-charge SOC at any given cycle. Between the 1st and the 80th cycles, the end-of-charge SOC was lowered by an estimated 8%, independent of discharge rate. In the case of C/1, the relaxed *cte*-OCV falls on the voltage plateau initially, making an accurate SOC tracing impossible. The change in the end-of-discharge SOC however was estimated at about 7.5% from the end-of-charge SOC and the charge return. From the variations in the end-of-discharge and end-of-charge SOCs, a 7% reduction in the SOC range was observed for the C/5 cycles. Similarly, a 3.5% reduction for C/2 cycles and 0.5% for C/1 cycles were observed. This rate-dependent SOC range reduction indicates that lower rates suffer more than the higher ones. This phenomenon explains the decrease in the Peukert constant between the 10th and the 80th cycle observed in Fig. 2(b).

According to the analysis in the second stage where the loss of Li inventory was the major cause of the capacity fading, we can hypothesize that it would have been already taking place in the first stage of degradation. From Fig. 8, we also observed that no loss of active material occurred in this stage, as incremental capacity peak intensities remain similar over the first 80 cycles. Interpreting from the same incremental capacity curves, we also concluded that there was no evidence of under-discharge or under-charge. It is therefore apparent that the loss of Li inventory is solely responsible for the end-of-charge SOC decline in this stage.

The fact that the lower rates suffer more capacity loss seems somehow counter-intuitive. The floating charge algorithm is equivalent to a C/20 charge. At such a low rate nearly all the available Li ions are retained in the negative electrode at the end-of-charge. At the end-of-discharge, the extent of Li depletion in this electrode is depending on the discharge regimen, as exhibited in Fig. 10. The unused Li ions are considered the "reserved" capacity, which plays an interesting role in the capacity degradation. As loss of Li inventory occurs, as induced by the side reactions in the cycle aging [5,6,9,24], the amount of Li ions returns to the negative electrode in charging, and thus the "reservoir" of Li, continues to decrease over cycles. This is reflected in the decline of the end-of-charge SOC. This result however cannot explain the observed rate-dependence of capacity loss in this stage.

We should point out here that it is peculiar to observe the rate-dependence in the continuous decline of the end-of-discharge SOC in the first 80 cycles. The decline in the end-of-discharge SOC implies that each consecutive cycle reaches a lower SOC to allow the maximum capacity be achieved at a given rate. Since the Li reservoir is reducing, as induced by the loss of Li inventory, it becomes logical now to realize that such a maximum capacity can be achieved by tapping into the "reserved" Li for the given rate. It is therefore conceivable that the lower rates shall have less "reserved" Li, thus they should consume their "reserved" Li faster than the higher ones. This rate-dependent consumption of "reserved" Li explains why the lower rates exhibit more capacity loss than the higher ones. Fig. 12

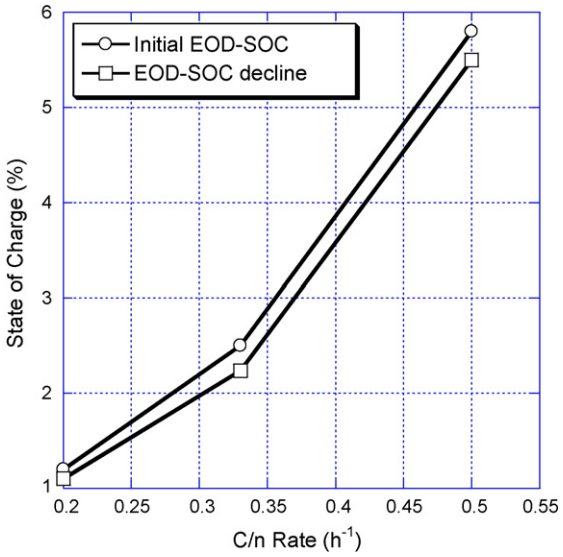

Fig. 12. Correspondence of the rate-dependence in the initial end-of-discharge SOC and the eventual decline in the end-of-discharge SOC over the first 80 cycles at various rates.

shows the correspondence of the rate-dependence of the initial end-of-discharge SOC and the eventual decline in end-of-discharge SOC over the first 80 cycles at various rates. Such a close correspondence reflects exactly what we would expect from the consumption of the "reserved" Li in the negative electrode. Interestingly, considering a 8% loss due to loss of Li inventory after 80 cycles, thus a 0.1% per cycle; the "reserved" Li would have been depleted after 15 C/5 cycles, 55 C/2 cycles, or after 80 C/1 cycles. It is now clear why the C/1 capacity is stable until the 80th cycle, as observed in Fig. 1, while the others are decreasing.

4.3.3. Stage three of capacity retention

The increase of the polarization resistance (in Fig. 9) did not appear to bear any major influence on the capacity loss in the first 400 cycles, although one may suspect that it could cause under-discharge (Fig. 8), judging from the increase in the end-of-discharge relaxed cell voltage (Fig. 6(a)) and end-of-discharge SOC (Fig. 11).

Figs. 6(a) and 11 also help us to verify that there was some loss of active material in the cycle aging. First, in Fig. 6(a) we noticed that the end-of-charge relaxed cell voltage is rather constant throughout the entire cycle aging, which indicates that the cell has been on a voltage plateau as indicated in Fig. 6(b). This constant voltage is established by the difference between the $LiFePO_4$–$FePO_4$ plateau at the positive electrode and the LiC_6–LiC_{12} plateau at the negative electrode. From the *pseudo*-OCV versus SOC curve (Fig. 5), we determined that this plateau spans about 30% of the available capacity. This plateau capacity is presented by the gray area in Fig. 11. As long as the end-of-charge relaxed cell voltage remains constant, the end-of-charge SOC must be staying within the gray area. After 450 cycles, we however found that the end-of-charge SOC began to reach outside the gray area; i.e., below the lower boundary of the gray area plateau. This result prompts us to postulate that some of the active material must have been lost during aging. This explanation is intriguing because the loss of active material (on one of the two electrodes) should have led to a less amount of (equivalent) active material involved in cycling, thus the same amount of Li for intercalation now should be available for a less amount of active material. Such an "artificial enrichment" of Li concentration in the reaction would make the grains that remain active now retain a higher end-of-charge SOC, which helps the cell voltage remain in the voltage plateau as reflected in Fig. 6(a). Loss of active material is likely due to localized grain isolation by an inorganic surface film, as suggested in [24]. As we have mentioned in stage two that loss of active material likely has occurred already, but it was difficult to quantify. In this stage, the evidence becomes quantifiable. If the loss of active material were responsible for the capacity discrepancy as reflected in the difference between the range of the plateau and that indicated by the end-of-charge SOC variation, it would account for at least 15% after 600 cycles.

It is also brought to our attention that after 580 cycles C_5 is less than C_3 as shown in Fig. 2(a), while the end-of-discharge relaxed cell voltage for C/5 is lower than that of C/3. This observation seems unrelated to data scattering, because the test results reflect consistent behavior for 3 cycles at each rate. In addition, this reverse trend only started from the 500th cycle, where C_5 was peculiarly low, even though it was still higher than C_3. This discrepancy between capacity and corresponding SOC change indicates that the loss of active material and loss of Li inventory may attribute concomitantly yet differently in proportion to such discrepancy with rate dependency. First, the extent of loss of active material or loss of Li inventory is reflected in the state of the cell disregarding the rate. Thus, at any point in life, the difference between C_5 and C_3 cannot be due to the difference in the extent of loss of active material or loss of Li inventory. The lower end-of-discharge SOC and capacity at C/5 than at C/3 indicates that the SEI reforming is rate-dependent and creating a severe interface kinetic issue that is worse at a lower rate, resulting in a lower capacity with a lower end-of-discharge SOC.

4.3.4. Summary of the degradation mechanisms

Although the degradation mechanisms appeared complex at first, the above *in situ* incremental capacity analysis and SOC tracing revealed that they are mainly the result of an underlying process, the complex growth of a Li-consuming SEI layer formation. The direct consequence of this process is the loss of Li inventory for capacity retention. Its continuous growth also increases the polarization resistance of the cell. Although this resistance increase was not reflected in the capacity loss at first because of little cell reaction occurring near the end of the potential window, the resistance increase eventually induced under-discharge towards the end-of-life in the cell, especially for higher rates. Concurrently, this SEI layer growth also caused isolation to some grains, which become inactive when the SEI layer becomes too thick, leading to the loss of active material (estimated for at least 15% at the end-of-life). Fortunately, no under-charge was observed due to the benefit of C/20 trickle charge.

5. Conclusion

By using incremental capacity and *cte*-OCV analyses on a $LiFePO_4$ commercial cell cycle aging test we were able to decipher the main contribution to the capacity fading due to the loss of lithium inventory, followed by the loss of active material. After 400 cycles under-discharging starts to take the toll at higher rates. This study exemplifies the potential and utility of this *in situ*, non-invasive analysis capability provided by the combined approach. The details revealed by these analyses provide more detailed understanding of degradation than that achieved by just monitoring the increase of the cell internal resistance.

Although this *in situ* approach could not provide direct and definitive physical evidence on the degradation mechanism, it could however provide substantial indirect inference to the degradation pathway from a limited set of experimental data typically received in cycle life testing. Carefully deriving such information can be very beneficial for on-board diagnosis and prognosis of the battery, which can help improve battery (pack) management, reliability, safety, and the operation of the battery pack.

Acknowledgments

This work is performed under a contract with the Hawaii Center for Advanced Transportation Technologies (HCATT) with the support from the U.S. Air Force Advanced Power Technology Office (APTO) at the Robins Air Force Base in Georgia. The authors would also like to thank Ruey Hwu and Vojtech Svoboda for carrying out part of the experimental work.

References

[1] S.-Y. Chung, J.T. Bloking, Y.-M. Chiang, Nat. Mater. 1 (2002) 123.
[2] A.K. Padhi, K.S. Najundaswamy, J.B. Goodenough, J. Electrochem. Soc. 144 (1997) 1188.
[3] A.S. Andersson, J.O. Thomas, B. Kalska, L. Häggström, Electrochem. Solid State Lett. 3 (2000) 66.
[4] H. Huang, S.-C. Yin, L.F. Nazar, Electrochem. Solid State Lett. 4 (2001) A170.
[5] K.A. Striebel, A. Guerfi, J. Shim, M. Armand, M. Gauthier, K. Zaghib, J. Power Sources 119–121 (2003) 951.
[6] J. Shim, K.A. Striebel, J. Power Sources 119–121 (2003) 955.
[7] K. Zaghib, K.A. Striebel, A. Guerfi, J. Shim, M. Armand, M. Gauthier, Electrochim. Acta 50 (2004) 263.
[8] J. Vetter, P. Novĭak, M.R. Wagner, C. Veit, K.-C. Möller, J.O. Besenhard, M. Winter, M. Wohlfahrt-Mehrens, C. Vogler, A. Hammouched, J. Power Sources 147 (2005) 269–281.
[9] K. Striebel, J. Shim, A. Sierra, H. Yang, X. Song, R. Kostecki, K. McCarthy, J. Power Sources 146 (2005) 33–38.
[10] http://www.uscar.org/guest/publications.php.
[11] M. Dubarry, B.Y. Liaw, J. Power Sources, submitted for publication.
[12] M. Dubarry, V. Svoboda, R. Hwu, B.Y. Liaw, Electrochem. Solid State Lett. 9 (2006) A454.
[13] M. Dubarry, V. Svoboda, R. Hwu, B.Y. Liaw, J. Power Sources 165 (2007) 566.
[14] M. Dubarry, V. Svoboda, R. Hwu, B.Y. Liaw, J. Power Sources 174 (2007) 366.
[15] J. Barker, R. Koksbang, M.Y. Saidi, Solid State Ionics 89 (1996) 25.
[16] J. Barker, M.Y. Saidi, R. Koksbang, Electrochim. Acta 41 (1996) 2639.
[17] J. Barker, Electrochim. Acta 40 (1995) 1603.
[18] A. Yamada, H. Koizumi, S. Nishimura, N. Sonoyama, R. kanno, M. Yonemura, T. Nakamura, Y. Kobayashi, Nat. Mater. 5 (2006) 357.
[19] L. Laffont, C. Delacourt, P. Gibot, M.Y. Wu, P. Kooyman, C. Masquelier, J.M. Tarascon, Chem. Mater. 18 (2006) 5520.
[20] C. Delmas, M. Maccario, L. Croguennec, F. Le Cras, F. Weill, Nat. Mater. 7 (2008) 665.
[21] T. Ohzuku, Y. Iwakoshi, K. Sawai, J. Electrochem. Soc. 140 (1993) 2490–2498.
[22] N. Meethong, H-Y.S. Huang, S.A. Speakman, W.C. Carter, Y.-M. Chiang, Adv. Funct. Mater. 17 (2007) 1115–1123;
N. Meethong, H-Y.S. Huang, W.C. Carter, Y.-M. Chiang, Electrochem. Solid State Lett. 10 (2007) A134–A138.
[23] C. Jiang, M. Wei, Z. Qi, T. Kudo, I. Honma, H. Zhou, J. Power Sources 166 (2007) 239–243.
[24] M. Koltypin, D. Aurbach, L. Nazar, B. Ellis, J. Power Sources 174 (2007) 1241–1250.
[25] F. Tanguy, J. Gaubicher, P. Soudan, N. Bourgeon-Martin, V. Mauchamp, D. Guyomard, Electrochem. Solid-State Lett. 10 (2007) A184.